Check for updates

Numerical modelling of the KOBO extrusion process using the Bodner–Partom material model

Marta Wójcik ⬢ · **Andrzej Skrzat** ⬢

Abstract Numerical simulations of the extrusion process assisted by die cyclic oscillations (KOBO extrusion) is presented in this paper. This is highly non-linear coupled thermo-mechanical problem. The elastic-viscoplastic Bodner–Partom-Partom material model, assuming plastic and viscoplastic effects in a wide range of strain rates and temperatures, has been applied. In order to perform simulations, the user material procedure for B–P material has been written and implemented in the commercial FEM software. The coupled Eulerian–Lagrangian method has been used in numerical computations. In CEL method, explicit integration of the constitutive equations is required and remeshing is not necessary even for large displacements and large strains analyses. The results of numerical simulations show the heterogeneous distribution of stress and strain inside container and the non-uniform distribution of strain in the extruded material. The increase of material temperature has been noted. The results obtained (stress,

temperature, location of plastic zones) qualitatively confirm the results of experimental investigations. The application of the user material procedure allows accessing all material state variables (current yield stress, hardening parameters, etc.), and therefore it gives detailed information about phenomena occurring in extruded material inside recipient. This information is useful for a proper selection of parameters of the KOBO extrusion process e.g. synchronization of the punch displacement with the die oscillations frequency to avoid the saturation of material isotropic hardening, which blocks the progress of extrusion.

List of symbols

α	Linear expansion coefficient [−]
β_{ij}	Tensorial quality value [−]
$\dot{\beta}_{ij}$	Rate of tensorial quality value [1/s]
ε_{ij}	Total strain [−]
$\varepsilon_{ij}{}^{(e)}$	Elastic strain [−]
$\varepsilon_{ij}{}^{(ie)}$	Inelastic (plastic) strain [−]
$\dot{\varepsilon}_{kl}$	Strain rate [1/s]
$\dot{\varepsilon}_{ij}{}^{(ie)}$	Inelastic strain rate [1/s]
ξ	Position parameter [−]
η	Taylor-Quinney coefficient [−]

Marta Wójcik and Andrzej Skrzat contributed equally to this work.

M. Wójcik (✉) · A. Skrzat
Department of Materials Forming and Processing, Faculty of Mechanical Engineering and Aeronautics, Rzeszow University of Technology, 8 Powstańców Warszawy Ave., 35-959 Rzeszów, Poland
e-mail: m.wojcik@prz.edu.pl

A. Skrzat
e-mail: askrzat@prz.edu.pl

η_w	Viscosity parameter
λ	Plastic multiplier [−]
ν	Poisson's ratio [−]
ρ	Density [kg/m^3]
$\boldsymbol{\sigma}$	Cauchy stress tensor [Pa]
$\overset{\nabla G}{\boldsymbol{\sigma}}$	Green-Naghdi stress rate [Pa/s]
$\overset{\nabla J}{\boldsymbol{\sigma}}$	Jaumann stress rate [Pa/s]
$\dot{\boldsymbol{\sigma}}$	Stress rate in a corotational frame [Pa/s]
$\dot{\boldsymbol{\sigma}}_{ij}^{(e)}$	Elastic stress rate [Pa/s]
δ_{ij}	Kronecker delta function [−]
$\boldsymbol{\Phi}$	Flux function [m^3/s]
$\boldsymbol{\Omega}$	Angular velocity matrix [rad/s]
$\|\boldsymbol{\sigma}\|$	Norm of $\boldsymbol{\sigma}$
$\|\boldsymbol{\beta}\|$	Norm of $\boldsymbol{\beta}$
C_{ijkl}	Elastic stiffness tensor [Pa]
c_p	Specific heat [J/kg K]
$\boldsymbol{D}$	Velocity strain [s^{-1}]
D_0	Limiting shear-stress rate [s^{-1}]
e	Strain energy [J]
E	Young modulus [Pa]
h	Thermal conductivity [W/m·K]
J_2	Second invariant of the deviatoric stress [Pa]
m_1	Hardening rate coefficient for isotropic hardening [Pa^{-1}]
m_2	Hardening rate coefficient for kinematic hardening [Pa^{-1}]
n	Strain rate sensitivity parameter [−]
$\dot{p}$	Viscoplastic strain rate [s^{-1}]
$\dot{p}_0$	Initial viscoplastic strain rate [s^{-1}]
r_1	Recovery exponent of isotropic hardening [−]
r_2	Recovery exponent of kinematic hardening [−]
s_{ij}	Deviatoric stress tensor [Pa]
S	Source term
q	Heat volume rate [J/K m^3]
W	Spin tensor [s^{-1}]
$\dot{W}_p$	Plastic work rate [J/m^3 s]
x	Backstress in kinematic hardening [Pa]

Z	Internal state variable [Pa]
Z^I	Isotropic component of Z [Pa]
Z^D	Directional (kinematic) component of Z [Pa]
Z_0	Initial value of the isotropic hardening variable [Pa]
Z_1	Limiting (maximum) value for isotropic hardening [Pa]
Z_2	Fully recovered (minimum) value for isotropic hardening [Pa]
Z_3	Limiting (maximum) value for kinematic hardening [Pa]
$\dot{Z}^I$	Rate of isotropic component [Pa/s

Abbreviations	B–P	Bodner–Partom model
	CEL	Coupled Eulerian–Lagrangian method
	VF	Volume fraction

1 Introduction

The development of material forming processes over years and their application in many industrial sectors caused the need of proper description of the material behaviour at very high strain rates, up to even 5000–11,000 s^{-1} [1, 2]. The determination of material properties at high strain rates is complicated and restricted by the ambiguity of the methods used, as well as by the complexity of the strain phenomenon. The mechanical properties of materials at strain rates above 10 s^{-1} might be determined with the use, e.g. of the split Hopkinson pressure bar test, a Taylor impact, a shock loading by plate impact and a high-speed photography, whose usage is limited by the equipment availability [3].

In numerical simulations, the description of the material behaviour subjected to loading at high strain rates requires the selection of a proper material model. The classical plasticity theory, in which the constitutive equations are time-independent or time-dependent, might be applied in a solution of many engineering problems. In forming processes involving large deformations and large strains, the unified plasticity theory has indicated sustainability for use. The unified plasticity theory, which is related to both elasticity and plasticity theories, is used to model the behaviour of

material under loading for a wide range of temperature and strain rates including their dependence on time [4]. The unified theory does not include the yield condition typical for the classical plasticity one. The lack of yield condition eliminates the need of judgement of loading/unloading conditions [5]. The long-term material response can be considered for different loading conditions (creep and the relaxation) [6]. In the unified plasticity theory, both elastic and inelastic responses occur simultaneously. As in classical plasticity of metals, the elastic and inelastic strains are additive for all stages of loading and unloading [6, 7].

The classical plasticity in macroscopic scale applies differential constitutive equations, e.g. the plastic flow rule to describe the material model. The microscopic phenomena responsible for the plastic deformation, i.e. the dislocation slip and its formation, as well as the grow of twins—are not considered here. Therefore, the classical plasticity theory can model the changes in a material microstructure on the macroscopic level only. In contrast, the micro-mechanisms of plastic deformation are considered in a unified plasticity theory. The dislocation slip, which is mainly responsible for the plasticity in solids, can be analyzed in a macroscopic scale. The continuum body divided into macroscopic points (grains) can be described by the unified plasticity which examines the response of all macroscopic grains in a solid as their irreversible macroscopic movement with a certain direction caused by the dislocation slip [8].

The behaviour of materials subjected to loading over a wide range of strain rates and temperatures is described using different phenomenological and physical models, e.g. power law [9], Zerilli-Armstrong [10], Rusinek-Klepaczko [11–13], Nemat-Nasser [14], Follansbee-Kocks [15, 16], Johnson–Cook [17–20], Miller [21], Bodner [22], Walker [23], Kocks [24] and Krempl [25]. These models include the hardening effects and static or dynamic recovery in different way. The viscosity functions of selected unified viscoplastic models are contained in Table 1.

The viscoplastic constitutive model proposed by Miller assumes both isotropic and kinematic hardening by the addition of one backstress for kinematic hardening and a drag stress for isotropic one [21]. It does not include yield stress and the viscosity function is a combination of a hyperbolic sine and a power law [31]. The Robinson model proposed first by Robinson and developed by Arnold and Saleeb [32] and Saleeb

Table 1 The comparison of viscosity functions for different unified viscoplastic models

Model	Viscoplastic strain rate $\dot{p}$
Miller [21]	$\dot{p} = B\left[sinh\left(\frac{\sigma}{D}\right)^{1.5}\right]^n$ (1)
Delobelle [23]	$\dot{p} = A sinh\left(\frac{\sigma}{D}\right)^n$ (2)
Kocks [24]	$\dot{p} = \dot{p}_\infty \exp\left[-\frac{1}{C}\langle 1 - \left(\frac{\sigma}{D}\right)^p \rangle^q\right]$ (3)
Johnson–Cook [17–20]	$\dot{p} = \dot{p}_0 exp\left[-\frac{1}{C}\left(\frac{\sigma}{D} - 1\right)\right]$ (4)
Krempl [25]	$\dot{p} = \frac{\sigma}{Ek_1}\left(1 + \frac{\sigma}{k_2}\right)^{k_3}$ (5)
Onera exponential [26]	$\dot{p} = \left(\frac{\sigma}{D}\right)^n exp\left(\alpha\left(\frac{\sigma}{D}\right)^{n+1}\right)$ (6)
Onera double slope [27]	$\dot{p} = \left(\frac{\sigma}{D}\right)^n\left[1 + \left(\frac{\sigma}{q}\right)^\alpha\right]$ (7)
Perzyna [28–30]	$\dot{p} = \frac{\langle \phi(f) \rangle}{\eta_w} \boldsymbol{m}$ (8)

[33] introduces a backstress for a kinematic hardening, a drag stress for an isotropic one, a yield stress and a power function for a viscoplastic flow. Additionally, the model assumes a static recovery term without introducing a dynamic one as in other viscoplastic models [31]. The main disadvantage of this model is so-called "indifferent character" of the kinematic hardening resulting in vanish of previous backstress in further tension or compression tests. It causes that the subsequent tension results in exactly the same response of a material as in the initial tension cycle [34].

The Walker unified viscoplastic model does not contain a yield stress and includes both isotropic and kinematic hardening which are described as a drag stress and the backstress evolution, respectively. In the backstress equation, the special asymmetry is contained and the initial non-recoverable asymmetry of a viscoplastic behaviour of a material is included. The static recovery effect takes place only for the nonlinear backstress. In the Walker's equation, temperature rate terms for a backstress are introduced [31, 35].

In the model proposed by Krempl [25], the backstress evolution is formulated in terms of the total strain rate instead of the viscoplastic strain one. The dynamic recovery term included in this equation is proportional to the norm of a viscoplastic strain rate. The Krempl model also includes the hardening rate effects for the equilibrium stress.

The other unified viscoplastic constitutive equation described by Delobelle [23] is formulated as a hyperbolic sine and the backstress evolution is given by a secondary and tertiary backstresses. The drag stress defining the isotropic hardening is a function of a temperature and the accumulated plastic strain. The static recovery for the Delobelle model appears only in kinematic hardening [31, 36].

The Perzyna model [37] relates the viscoplastic strain rate to the specific function depending on the current stress and state variables which define the stress–strain history. The model includes only isotropic hardening without taking into consideration the kinematic one. It assumes a yield stress but it is relatively insensitive to the strain rate and a temperature.

In each of the mentioned unified viscoplastic models, there is no function describing the relationship between the stress or a viscous stress and the norm of the viscoplastic strain rate. The viscosity functions are often only modifications of the power law in Norton's equation for creep [31] where the n exponent varies with the stress or the strain rate [38].

Many of unified elastic-viscoplastic constitutive equations are limited to modelling of small strain problems. Their usefulness in engineering applications is restricted by difficulties with the identification of multiple material parameters. Among material models of the unified plasticity theory, the Bodner–Partom one become very popular in the eighties and nineties of the twentieth century.

The Bodner–Partom (B–P) unified plasticity model was formulated by S.R. Bodner and Y. Partom in 1975 in order to examine the nonlinear elastic-viscoplastic response of titanium alloy subjected to loading, assuming the strain hardening [39]. It is an elastic-viscoplastic model described by physical and phenomenological factors based on the continuum mechanics [40]. The B–P model takes into account the micromechanical effects, e.g. the dislocation dynamics in isothermal loading conditions, kinematic and isotropic hardening, the material damage, the relaxation and the creep [41, 42]. It was initially used to describe the behaviour of metal alloys under loading at elevated temperatures and for a wide range of strain rates [43, 44]. The basic equations were developed in order to consider implementations for non-metallic materials [45–47], e.g.; polymers [48–50], tissues [51], as well as architectural and technical fabrics [52, 53]. The model is also used for

sophisticated problems associated with the creep and the crack development of composites with a metal matrix [54]. In [55], the B–P model was applied to describe viscoelastoplastic properties and the deformation mechanism of a cement-emulsified asphalt mixture. Numerical simulations of the damage evolution for plastic-bonded explosives subjected to complex stress states are shown in [56]. The determination of viscoplastic parameters of a rubber-toughened plastics using the B–P model is presented in [57]. More detailed information about the B–P model and its application in numerical calculations for different materials is included in [58–63].

Due to the assumption of a wide range of strain rates and temperatures, the B–P model might be applied in numerical simulations of the material forming processes. In [64], it was used for modelling the conventional extrusion process. In this paper, for the first time the B–P model is applied in numerical simulations of the KOBO extrusion process. The KOBO method is an unconventional elastic–plastic deformation process classified to *Severe Plastic Deformation* (SPD) methods changing a plastic deformation by the introducing the die cyclic oscillations with a given frequency and a given angle (approximately 5°–7°) [65]. The die cyclic oscillations cause the change in material structure and lead to an increase in the concentration of lattice defects [66].

The reduction of the extrusion force and the plastic work, as well as the elimination of process annealing in comparison to the conventional extrusion are the main advantages of the KOBO method. The process allows the cold forming of heavily deformed materials and enables the stable processing of their structure to the even nanostructured size. The products with a complex geometry might be produced without significant tools wear [66, 67]. More detailed information about the KOBO extrusion process is contained in [66–71].

Numerical simulations of the KOBO extrusion can help to optimize the whole process in terms of the reduction of the extrusion force and the total operational costs. Reliable simulations can eliminate possible technical problems associated with the material continuous extrusion. In some laboratory tests material was not extruded at all, or it was extruded only a little, and then it was blocked in the die. Numerical simulations can predict such unwanted behaviour usually caused by a large isotropic hardening (up to

saturation) and can help to set-up extrusion process parameters to avoid such technical difficulties.

The modelling of the conventional extrusion process is shown in [72–74]. In [75], the numerical simulations of the standard extrusion process using the Eulerian–Lagrangian approach is presented. The results of the coupled Eulerian–Lagrangian (CEL) analysis were compared with the results of axisymmetric Lagrangian numerical analysis (the continuous remeshing was required) and with the experiment. The reasonable convergence between alternative numerical approaches and experimental data were obtained.

Although many papers dedicated to the conventional extrusion are published, there are very few numerical simulations available concerning the KOBO extrusion method. Most of them focus on the change of the material structure during the process. The evolution of the texture in the KOBO extrusion is contained in [76]. In [77] numerical analyses including the generation, interaction and annihilation of point defects in a KOBO method are shown. In [78], the numerical simulation of the KOBO extrusion for Chaboche-Lemaitre elastic–plastic model with isotropic and kinematic hardening is presented. The results show phenomena occurring in the extruded material, e.g. the ratcheting and the mean stress relaxation. The small amount of research dedicated to the modelling of the KOBO extrusion assuming the hardening of a material confirms the purposefulness of the works undertaken.

In simulations of KOBO extrusion process presented in this paper, the coupled thermo-mechanical CEL approach including the heat generation due to the plastic deformation has been used. Since B–P material model is not implemented in commercial FEM programs, the user material procedure VUMAT has to be written, compiled and linked to Simulia Abaqus progam used here in numerical computations.

2 The Bodner–Partom unified elastic-viscoplastic material model

The KOBO extrusion is a complex process leading to the occurrence of high stresses and strains in a material. Material model appropriate for cyclic loading considering kinematic and isotropic hardening should be used in numerical calculations. Material model also ought to take into account the change of a temperature and its influence on the elastic-viscoplastic plastic response.

The Bodner–Partom (B–P) material model applied in simulations is based on three fundamental relationships [41]:

(1) The plastic flow rule relates the inelastic strain rate $\dot{\varepsilon}_{ij}^{(ie)}$ with the deviatoric stress using the plastic multiplier λ (Eq. 9).

$$\dot{\varepsilon}_{ij}^{(ie)} = \lambda s_{ij} \tag{9}$$

where s_{ij} is deviatoric stress tensor (Eq. 10)

$$s_{ij} = \sigma_{ij} - \frac{1}{3}\sigma_{kk}\delta_{ij} \tag{10}$$

where δ_{ij} is Kronecker delta function.

(2) The kinetic equation relates the plastic multiplier with the stress invariants using internal state variables.

(3) The evolution law defines the changes of the internal state variables ($\dot{Z}^I$ and $\dot{\beta}_{ij}$).

The B–P model allows taking into consideration simultaneously elastic and plastic effects, isotropic and kinematic hardening, viscoplasticity, creep, as well as the relaxation for a wide range of temperatures and strain rates [79]. The model is described by the following constitutive equations:

(1) The superposition of elastic and inelastic strains (Eq. 11):

$$\varepsilon_{ij} = \varepsilon_{ij}^{(e)} + \varepsilon_{ij}^{(ie)} \tag{11}$$

where ε_{ij} is the total strain, $\varepsilon_{ij}^{(e)}$ is the elastic strain and $\varepsilon_{ij}^{(ie)}$ is the inelastic (plastic) strain.

(2) The elastic stress rate $\dot{\sigma}_{ij}^{(e)}$ obtained from the time derivative of the generalized Hooke's law (Eq. 12):

$$\dot{\sigma}_{ij}^{(e)} = C_{ijkl}(\dot{\varepsilon}_{kl} - \dot{\varepsilon}_{kl}^{(ie)}) \tag{12}$$

where $\dot{\varepsilon}_{kl}$ and $\dot{\varepsilon}_{kl}^{(ie)}$ are the total and inelastic strain rates, respectively and C_{ijkl} is the elastic stiffness tensor according to the Hooke's generalized law.

(3) The inelastic strain rate (Eq. 13):

$$\dot{\varepsilon}_{ij}^{(ie)} = \sqrt{\frac{D_0^2}{J_2 exp\left(-\left(\frac{Z^2}{3J_2}\right)^n\right)}} s_{ij} \qquad (13)$$

where D_0 and n are the B–P material parameters, Z_0 is the initial value of the isotropic hardening variable, Z is the internal state variable and J_2 is the second invariant of the deviatoric stress.

(4) The incompressibility condition for inelastic deformations (Eq. 14):

$$\varepsilon_{kk}^{(ie)} = 0 \qquad (14)$$

(5) Plastic multiplier is (Eq. 15) [80]:

$$\lambda = \sqrt{\frac{D_0^2}{J_2 \exp\left(-\left(\frac{Z^2}{3J_2}\right)^n\right)}} \qquad (15)$$

The B–P material behaviour under loading is described using temperature dependent and independent parameters.

The internal state variable Z in Eq. 13 represents the material resistance to the inelastic flow at the current state. It is the superposition of isotropic Z^I and directional (kinematic) Z^D components in line with Eq. 16:

$$Z = Z^I + Z^D \qquad (16)$$

The Z^I depends on the load history and its evolution is defined as follows (Eq. 17):

$$\dot{Z}^I = m_1\left(Z_1 - Z^I\right)\sigma_{ij}\dot{\varepsilon}_{ij}^{(ie)} - A_1 Z_1 \left(\frac{Z^I - Z_2}{Z_1}\right)^{r_1} \qquad (17)$$

The $A_1 Z_1 \left(\frac{Z^I - Z_2}{Z_1}\right)^{r_1}$ part of Eq. 17 is a softening or the static recovery caused by the low strain rates at relatively low temperatures. If the static recovery does not occur, the Z_1 equals the Z saturated value.

The Z^D parameter depends on the load history and the β_{ij} tensorial quantity value is related with the directional component of the hardening in the direction of current stress $\sigma\left(\beta_{ij}\right)$ (Eq. 18).

$$Z^D = \beta_{ij}\left(\frac{\sigma_{ij}}{\|\beta_{ij}\|}\right) \qquad (18)$$

where

$$\dot{\beta}_{ij} = m_2 \left(Z_3\left(\frac{\sigma_{ij}}{\|\sigma_{ij}\|}\right) - \beta_{ij}\right)\sigma_{ij}\dot{\varepsilon}_{ij}^{(ie)} - A_2 Z_1 \left(\frac{\|\beta_{ij}\|}{Z_1}\right)^{r_2}\left(\frac{\beta_{ij}}{\|\beta_{ij}\|}\right) \qquad (19)$$

The proper selection of the B–P material parameters enables to obtain an appropriate material response under external load. The detailed procedure for the determination of the B–P material parameters is described in [81, 82]. Other research can be found in [83, 84]. In last thirty years, the B–P model has been extensively examined and values of material constants for different materials are available in the literature, therefore. The data for AMG-6 alloy considered here for 20, 300 and 400 °C is taken from [63].

From the computational point of view, the KOBO extrusion is a coupled thermo-mechanical process in which the plastic deformation and the friction between tools and extruded material are the heat sources. The heat generation caused by the plastic deformation is calculated using the following equation (Eq. 20):

$$q = \eta(\boldsymbol{\sigma} - \boldsymbol{x}) : \dot{\boldsymbol{\varepsilon}}^{(ie)} \qquad (20)$$

where q is the heat volume rate and $\dot{\boldsymbol{\varepsilon}}^{(ie)}$ is the inelastic strain rate, $\boldsymbol{\sigma}$ is the Cauchy stress, $\boldsymbol{x}$ is a back-stress associated with the kinematic hardening and η is a Taylor-Quinney coefficient. The Taylor-Quinney coefficient might be determined experimentally by processing thermal measurements. The constant averaged value is commonly applied in numerical simulations [85]. The Taylor-Quinney coefficient $\eta = 0.9$ has been used in this work. The increase of a temperature in a material in a wake of a heat generated during the high strain rate plastic deformation might be calculated using the following formula (Eq. 21):

$$\Delta T = \left(\frac{\eta}{c_p \rho}\right)\int_0^{\varepsilon^{(ie)}} (\boldsymbol{\sigma} - \boldsymbol{x}) : \dot{\boldsymbol{\varepsilon}}^{(ie)} \qquad (21)$$

where c_p is a specific heat and ρ is density.

It is very important that the user material subroutine written for large displacements and large strains should consider the rotation of the coordinate system. In Simulia ABAQUS, constitutive equations are defined in the corotational frame which enforces the use of objective stress rates namely: Jaumann or Green-Naghdi.

The Jaumann stress rate tensor $\overset{\triangledown J}{\boldsymbol{\sigma}}$ is defined as (Eq. 22) [65]:

$$\overset{\triangledown J}{\boldsymbol{\sigma}} = \dot{\boldsymbol{\sigma}} + \boldsymbol{\sigma}\boldsymbol{W} - \boldsymbol{W}\boldsymbol{\sigma} \tag{22}$$

where $\dot{\boldsymbol{\sigma}}$ is stress rate tensor in a corotational frame, $\boldsymbol{\sigma}$ is Cauchy stress tensor and $\boldsymbol{W}$ is spin tensor which comprises both the deformation and the rotation.

In the Jaumann rate, the $\dot{\boldsymbol{\sigma}}$ term is associated with the material deformation and the next two terms—$\boldsymbol{\sigma}\boldsymbol{W}$ and $\boldsymbol{W}\boldsymbol{\sigma}$ result from the rotation of the coordinate system. In ABAQUS program, the Jaumann stress rate is used for commercially implemented material models.

The Green-Naghdi rate $\overset{\triangledown G}{\boldsymbol{\sigma}}$ of the Cauchy stress is (Eq. 23) [86]:

$$\overset{\triangledown G}{\boldsymbol{\sigma}} = \dot{\boldsymbol{\sigma}} + \boldsymbol{\sigma}\boldsymbol{\Omega} - \boldsymbol{\Omega}\boldsymbol{\sigma} \tag{23}$$

where $\boldsymbol{\Omega}$ is the angular velocity matrix resulting from a rigid body rotation. Similarly to the Jaumann stress rate, the Green-Naghdi rate contains a term associated with the deformation ($\dot{\boldsymbol{\sigma}}$) and two terms which are related to the rotation ($\boldsymbol{\sigma}\boldsymbol{\Omega} - \boldsymbol{\Omega}\boldsymbol{\sigma}$).

In ABAQUS program, the Green-Naghdi rate of the Cauchy stress is applied as a default for the user-defined materials. Thus, the results obtained for the user-defined material model and material model implemented commercially may differ because of various objective stress rates used. It is worth highlighting that it is possible to apply the Jaumann stress rate for the user-defined material model. The Green-Naghdi stress rate might be expressed by means of the Jaumann rate as follows (Eq. 24):

$$\overset{\triangledown G}{\boldsymbol{\sigma}} = \overset{\triangledown J}{\boldsymbol{\sigma}} - \boldsymbol{\sigma}(\boldsymbol{W} - \boldsymbol{\Omega}) + (\boldsymbol{W} - \boldsymbol{\Omega})\boldsymbol{\sigma} \tag{24}$$

After substitution of Eq. 24 into Eq. 23, one can get Eq. 25.

$$\dot{\boldsymbol{\sigma}} = \overset{\triangledown J}{\boldsymbol{\sigma}} + \boldsymbol{W}\boldsymbol{\sigma} - \boldsymbol{\sigma}\boldsymbol{W} \tag{25}$$

Enforcing the Jaumann stress rate for the user-defined material model might be helpful in testing the correctness of user material procedures in elastic–plastic benchmark tests involving large displacements and rotations.

3 The explicit integration of the Bodner–Partom constitutive equations

The explicit integration (the Euler forward method) algorithm for the Bodner–Partom model using Eq. 12–20 is made in the user material procedure. The subscript for time t has been omitted in this paper. The components of the strain increment are the input data. The procedure determines the increment of the inelastic strain and updates the stress at the end of the integration step. The algorithm of the explicit integration for the B–P model is as follows:

(1) The determination of Z^I state variable for time $t + \Delta t$ (Eq. 26):

$$\left. \begin{array}{c} \dot{Z}^I = m_1\left(Z_1 - Z^I\right)\dot{W}_p - A_1 Z_1\left(\frac{Z^I - Z_2}{Z_1}\right)^{r1} \\ \Delta Z^I = \dot{Z}^I \Delta t \\ Z^I(t = 0) = Z_0 \\ Z^I(t + \Delta t) = Z^I + \Delta Z^I \end{array} \right\} \tag{26}$$

where $\dot{W}_p$ is a plastic work rate—Eq. 27:

$$\dot{W}_p = \boldsymbol{\sigma} : \boldsymbol{\varepsilon}^{(ie)} \tag{27}$$

(2) The calculation of $\boldsymbol{\beta}$ state variable for time $t + \Delta t$ (Eq. 28):

$$\left. \begin{array}{c} \dot{\boldsymbol{\beta}} = m_2\left(Z_3\left(\frac{\boldsymbol{\sigma}}{\|\boldsymbol{\sigma}\|}\right) - \boldsymbol{\beta}\right)\boldsymbol{\sigma} : \boldsymbol{\varepsilon}^{(ie)} - A_2 Z_1\left(\frac{\|\boldsymbol{\beta}\|}{Z_1}\right)^{r2}\left(\frac{\boldsymbol{\beta}}{\|\boldsymbol{\beta}\|}\right) \\ \Delta\boldsymbol{\beta} = \dot{\boldsymbol{\beta}}\Delta t \\ \boldsymbol{\beta}(t + \Delta t) = \boldsymbol{\beta} + \Delta\boldsymbol{\beta} \end{array} \right\} \tag{28}$$

where the norms of tensorial values $\|\boldsymbol{\sigma}\|$ and $\|\boldsymbol{\beta}\|$ are as follows (Eq. 29):

$$\left. \begin{array}{c} \|\boldsymbol{\sigma}\| = \sqrt{\boldsymbol{\sigma} : \boldsymbol{\sigma}} \\ \|\boldsymbol{\beta}\| = \sqrt{\boldsymbol{\beta} : \boldsymbol{\beta}} \end{array} \right\} \tag{29}$$

(3) The determination of Z^D and Z state variables for time $t + \Delta t$ (Eq. 30):

$$\left. \begin{array}{c} Z^D(t + \Delta t) = \boldsymbol{\beta}(t + \Delta t) : \left(\frac{\boldsymbol{\sigma}}{\|\boldsymbol{\sigma}\|}\right) \\ Z(t + \Delta t) = Z^I(t + \Delta t) + Z^D(t + \Delta t) \end{array} \right\} \tag{30}$$

(4) The computation of inelastic (plastic) strain for time $t + \Delta t$ (Eq. 31)

$$\left.\begin{array}{c} \dot{\boldsymbol{\varepsilon}}^{(ie)} = \sqrt{\left(\dfrac{D_0^2}{J_2}\right)exp\left(-\left(\dfrac{Z^2}{3J_2}\right)^n\right)}\boldsymbol{s} \\ \Delta\boldsymbol{\varepsilon}^{(ie)} = \dot{\boldsymbol{\varepsilon}}^{(ie)}\Delta t \\ \boldsymbol{\varepsilon}^{(ie)}(t+\Delta t) = \boldsymbol{\varepsilon}^{(ie)} + \Delta\boldsymbol{\varepsilon}^{(ie)} \end{array}\right\} \qquad (31)$$

where $\boldsymbol{s}$ is a deviatoric stress tensor.

(5) The determination of stress for time $t + \Delta t$ (Eq. 32):

$$\left.\begin{array}{c} \dot{\boldsymbol{\sigma}} = \boldsymbol{C}\left(\dot{\boldsymbol{\varepsilon}} - \dot{\boldsymbol{\varepsilon}}^{(ie)}\right) \\ \Delta\boldsymbol{\sigma} = \dot{\boldsymbol{\sigma}}\Delta t \\ \sigma(t+\Delta t) = \sigma + \Delta\sigma \end{array}\right\} \qquad (32)$$

(6) At the end, the state variables $\boldsymbol{\beta}$, $\dot{\boldsymbol{\varepsilon}}^{(ie)}$ and Z^I are saved.

4 The coupled Eulerian-Lagrangian method

Solving problems of solid mechanics including large deformations is difficult and complicated with the use of displacement-based finite element method described by the Lagrangian formulation in which the movement of the continuum is specified as a function of the material coordinates and time [87, 88]. In the Lagrangian formulation, nodes move together with the material in time (Fig. 1a) [89]. The mesh distortions and contact conditions can lead to the problems with a convergence. In these cases Eulerian methods become more efficient than the Lagrangian ones.

In the Euler method, which is applied usually in fluid mechanics, the movement of a continuum is a function of spatial coordinates and time [65]. The Eulerian reference mesh remains undistorted and is used to track the motion of a material in the

Eulerian domain [18, 19]. The material can move through the fixed Eulerian mesh and the elements distortion does not occur (Fig. 1b).

The CEL method keeps advantages of Eulerian and Lagrangian approaches and is very effective for a solution of large deformations problems. In [90, 91], the coupled Eulerian–Lagrangian method has been applied for the modelling of orthogonal cutting. The application of the CEL method for the prediction of a residual stress in dissimilar friction stir welding of aluminum alloys is presented in [92]. The modelling of defects in a friction stir welding process using the CEL approach is described in [93]. In [94], the usefulness of the Coupled Eulerian–Lagrangian analysis in geotechnics is praised. The CEL method can be also applied in modelling of material forming processes. Numerical results of the extrusion process are contained in [95, 96]. The modelling of the KOBO extrusion process using the CEL method and the Chaboche-Lemaitre material model is described in [78].

In the CEL approach, bodies which undergo large deformations (processed material) are meshed with Eulerian elements and the stiff bodies (tools) are meshed with Lagrangian ones. The Eulerian material is tracked as it flows through the mesh by computing its volume fraction (VF) in the CEL analysis. Each Eulerian element is designated a percentage, which represents the portion of that element filled with a material. If the Eulerian element is fully filled, its VF is 1. The VF is 0 for elements which are not filled with the Eulerian material.

The Lagrangian mass, momentum and energy conservation equations in the Eulerian spatial formulation arranged into conservative forms as below (Eq. 33–35) [79, 97]:
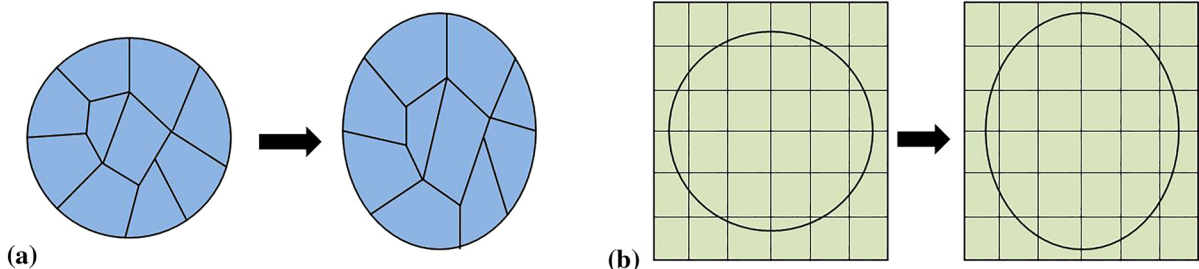

(a)   **(b)**

Fig. 1 The comparison of Lagrangian (**a**) and Eulerian (**b**) methods

$$\frac{\partial \rho}{\partial t} + \nabla \cdot (\rho v) = 0 \qquad (33)$$

$$\frac{\partial \rho v}{\partial t} + \nabla \cdot (\rho v \otimes v) = \nabla \cdot \boldsymbol{\sigma} + \rho \boldsymbol{b} \qquad (34)$$

$$\frac{\partial e}{\partial t} + \nabla \cdot (e v) = \boldsymbol{\sigma} : \boldsymbol{D} \qquad (35)$$

where ρ—the density, $\boldsymbol{\sigma}$—the Cauchy stress, $\boldsymbol{b}$—the vector of body forces, e—the strain energy, $\boldsymbol{D}$—he velocity strain.

The Eulerian governing equations above are written in the common general conservative form as follows (Eq. 36) [79, 97, 98]:

$$\frac{\partial \varphi}{\partial t} + \nabla \cdot \boldsymbol{\Phi} = S \qquad (36)$$

where $\boldsymbol{\Phi}$ is the flux function and S is the source term.

The solution of Eq. 36 can be divided into two stages (Eqs. 37 and 38) solved sequentially using the splitting operator. They represent Lagrangian and Eulerian steps, respectively. The Eq. 37, which represents the Lagrangian step, contains the source term and the Eulerian step described using Eq. 38 includes the convective one [97, 98].

$$\frac{\partial \varphi}{\partial t} = S \qquad (37)$$

$$\frac{\partial \varphi}{\partial t} + \nabla \cdot \boldsymbol{\Phi} = 0 \qquad (38)$$

The graphical scheme of the split operator is shown in Fig. 2. The deformed (Lagrangian) mesh is moved to the Eulerian fixed mesh and the volume of material transported between adjacent elements is computed. The Lagrangian solution variables, such

as the mass, energy, momentum, stress and others are then adjusted to account for the flow of the material between adjacent elements [78, 79].

The CEL method captures advantages of both the Lagrangian and Eulerian methods. The mesh is not deformed, and therefore the remeshing is not needed. A unique feature of the CEL method is that a single volume can be filled simultaneously with many materials which allows simulations of the extrusion of composites and porous materials [78]. The CEL approach also ensures better interpretation of contact conditions than the Eulerian method. The classical FEM methods based on the Lagrangian approach often cause the contact problems entailed by the distortion of the mesh.

5 Numerical simulations of the KOBO extrusion process

5.1 Numerical model

The 3D geometry model for the KOBO extrusion process is shown in Fig. 3. The tools are modelled as rigid bodies The 8-node linear Eulerian hexahedral elements considering thermomechanical coupling are used to mesh the Eulerian domain. The rectangular as well as cylindrical Eulerian domains with different mesh densities have been tested in simulations (Fig. 4). The Eulerian mesh covers the position of the material at the beginning of the process, and its location after the extrusion. Elastic and thermal material properties, as well as the FEM model data are contained in Table 2. The B–P model parameters for a
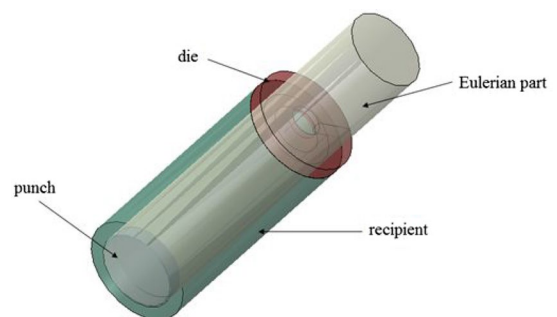
Fig. 2 The graphical interpretation of the split operator

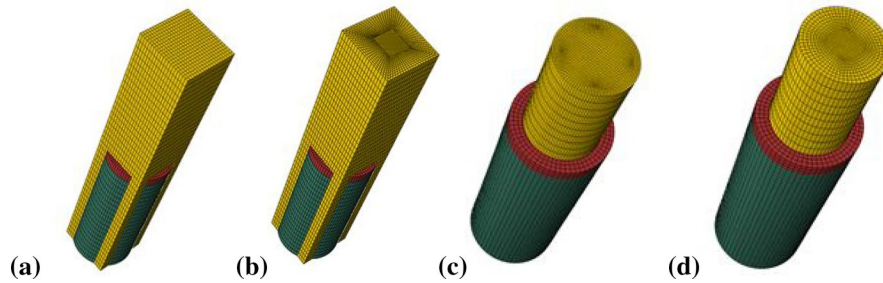**Fig. 3** The model of the KOBO extrusion process with a cylindrical Eulerian domain

Fig. 4 Meshes of the Eulerian part used in numerical simulations; rectangular Eulerian domain with regular density mesh (**a**), rectangular Eulerian domain with mesh thickening towards the core (**b**), rectangular Eulerian part with regular density mesh (**c**) and rectangular Eulerian part with mesh thickening to the core (**d**)

AMG-6 alloy for different temperatures are also listed in Table 2.

Numerical simulations of the KOBO extrusion process have been done in commercial Simulia ABAQUS program. The explicit integration procedure is required by ABAQUS in the CEL analysis. This integration method is conditionally stable—the stable time increment is very small [80]. The analysis of the KOBO extrusion requires hundreds of thousands time increments, and for this reason the problem cannot be solved in real process time. The mass scaling technique and the smooth step loading have been applied in order to speed up simulations and minimize the computation time [86, 100]. In order to decrease the computational costs, the time of real extrusion has been shortened in numerical simulations about one order. To avoid very large inertia forces caused by the sudden punch movement, the punch displacement has been smoothed from time t_0 to t_1 as described by Eq. 39 [101]:

$$u = u_0 + (u_1 - u_0)\xi^3(10 - 15 + 6\xi^2) \text{ for } t \in [t_0, t_1] \tag{39}$$

where ξ is a position parameter, u_0 is the initial punch position and u_1 is the final punch drive. In numerical simulations, $\xi = \frac{t - t_0}{t_1 - t_0}$ and $u_0 = 0$. The use of a smooth step amplitude in ABAQUS enables to apply and suppress the loads gradually.

5.2 Benchmark tests and simulations of KOBO extrusion

The proper selection of the B–P material model parameters is necessary to perform reliable numerical calculations of the KOBO extrusion process. Material parameters might be determined on the basis of experimental research, e.g. in tension or compression tests made for various strain rates. The determination of B–P parameters is out-of-scope of this paper. Since the Bodner–Partom material model is quite often used in solutions of various engineering problems, its constitutive parameters are available in literature for many typical materials. For B–P parameters given in Table 2 the following numerical benchmark tests have been done. Firstly, cyclic tension–compression tests have been made for temperatures of 20, 300 and 400 °C, respectively. The results are shown in Fig. 5. One can observe the isotropic and directional (kinematic) hardening as well as the stabilization of stress–strain curves after several cycles. The next numerical benchmark test presents the viscoplastic behavior of the B–P model. Simple tension tests have been made for various strain rates (0.001–100 [1/s]) and for temperatures of 20, 300 and 400 °C. The influence of the strain rate on the yield stress can be clearly seen in Fig. 6 for all considered temperatures.

Many simulations of the KOBO extrusion process have been made for various Eulerian meshes (cylindrical, rectangular), various mesh densities, different contact conditions (slip or no slip on die), etc. As the exemplary results, von-Mises stress distribution in the extruded material is shown in Fig. 7. This distribution is heterogeneous and the highest stress occurs near the die hole and next to the walls of the container. The stress decreases in the center of the recipient.

Figure 8 shows the equivalent plastic strain in the material subjected to the extrusion. The highest plastic strain values occur in corners of the recipient. One may notice that the material in a middle

Table 2 Parameters of the B–P model, other material parameters and details of the FEM model

Parameters for the B–P model			
Temperature-dependent parameters			
Parameter	Values for temperatures		
	20 °C	300 °C	400 °C
$n[-]$	2.06	2.0	1.9
$Z_0[MPa]$	324	306	280
$A_1[s^{-1}]$	0	$3.5 \cdot 10^{-3}$	0.15
$A_2[s^{-1}]$	0	$5.4 \cdot 10^{-2}$	0.99
Temperature-independent parameters			
$D_0[s^{-1}]$	10^4		
$Z_1[MPa]$	647		
$Z_2[MPa]$	35		
$Z_3[MPa]$	80		
$m_1[MPa^{-1}]$	0.182		
$m_2[MPa^{-1}]$	3.7		
$r_1[-]$	4.0		
$r_2[-]$	4.0		
Other material parameters			
Parameter	Value		
$E[Pa]$	71×10^9 for 20 °C		
	$55 \cdot 10^9$ for 300 °C		
	$48 \cdot 10^9$ for 400 °C		
$\nu[-]$	0.33		
$\rho[kg/m^3]$	2700		
$h[W/m \cdot K]$	206		
$\alpha[-]$	$4.5 \bullet 10^{-6}$		
$c_p[J/kg \cdot K]$	909		
FEM details			
Material model	Elastic-viscoplastic		
Integration procedure	Dynamic explicit		
Friction model	Coulomb model		
Friction coefficient	0.2		
Total number of variables in a model	114,558		
Stable time increment	$1.9 \bullet 10^{-7}$ s		

part of the container is in the elastic state (hydrostatic compression). Unfortunately, due to this fact, the B–P model is not computationally efficient. The elastic and inelastic strains are calculated in the whole domain for each load increment which significantly extends the computational time. On the other hand, elastic–plastic material models involving the yield condition are more effective from the point of computational costs since the elastic response requires much less computations than the plastic one.

It is important that the CEL approach in ABAQUS does not take into account the heat flow from the material to the tools cooled in experiments. Thus, the
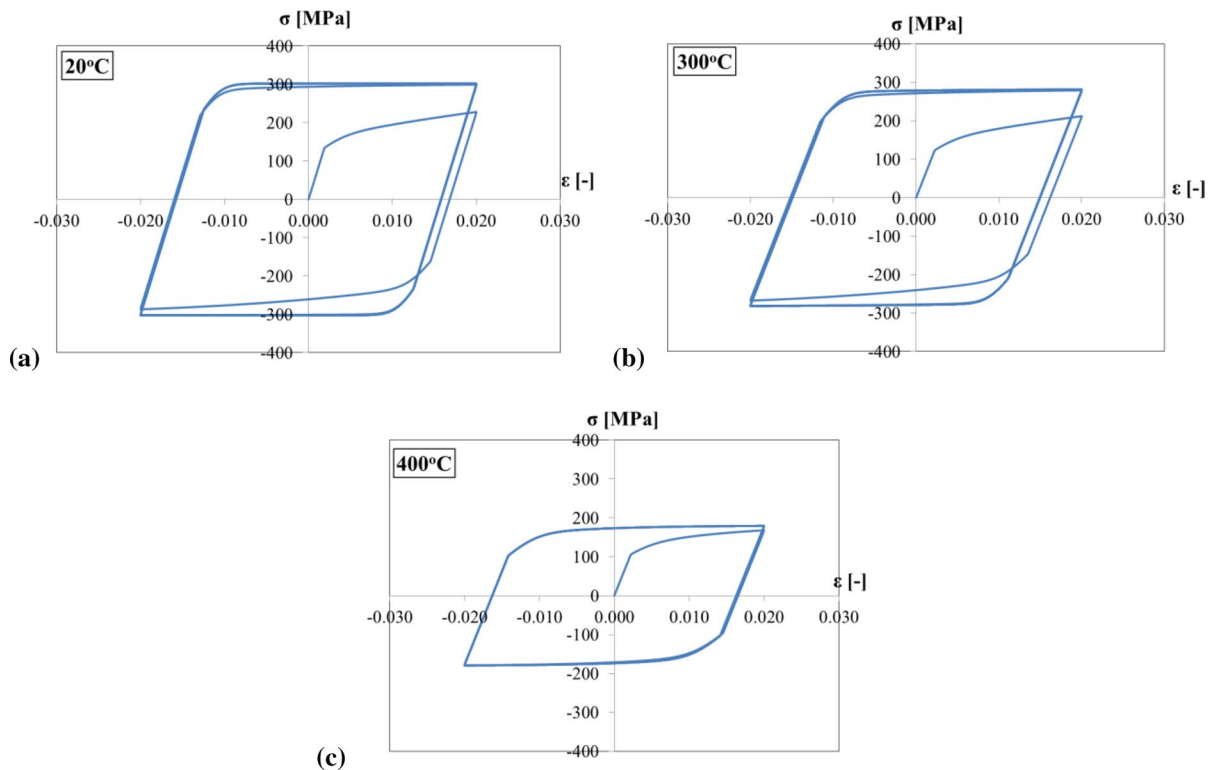
Fig. 5 Hysteresis curves obtained in cyclic loading tests for temperatures; 20 °C (**a**), 300 °C (**b**) and 400 °C (**c**)

computed temperature is more or less overestimated. In numerical simulations material parameters should be defined for the entire temperature range occurring in the analysis. The material softening with the increased temperature reduces the plastic work of the extrusion, and this way reduces the temperature raise.

The characteristic shape of plastic zones and streams of the plastic flow obtained numerically were confirmed in experimental investigations (Fig. 9). According to [102], the characteristic shape of lines of plastic flow is associated with the dominant crystal orientation which follows with the stream of the material.

The advantage of using material user subroutine over the material models commercially implemented in the FEM program is the possibility to obtain more information about the material response. Unlike in the commercially implemented material models, in the user procedures all isotropic and directional (kinematic) material hardening parameters are available and the influence of these parameters on the KOBO extrusion might be examined in this way.

Considering the KOBO process as a cyclic loading process, the ratcheting phenomenon should be taken into account. The ratcheting is characterized by the directional progressive accumulation of plastic deformation in a material under the non-symmetrical stress-controlled cyclic loading with non-zero mean stress [103, 104] without the load increase. Thus, the ratcheting is a very welcome phenomenon in the KOBO extrusion process. Unfortunately, the ratcheting used to stabilize after a certain number of loads, depending on the increase of the yield stress resulting from the isotropic hardening [105]. A large and dominant isotropic hardening can hamper a further deformation due to the cyclic load making the material response being almost only elastic. Detailed knowledge about the material hardening characteristic is very useful in optimization of the KOBO process in selection of appropriate frequency and the amplitude of the die oscillations in order to avoid the raise the isotropic hardening.
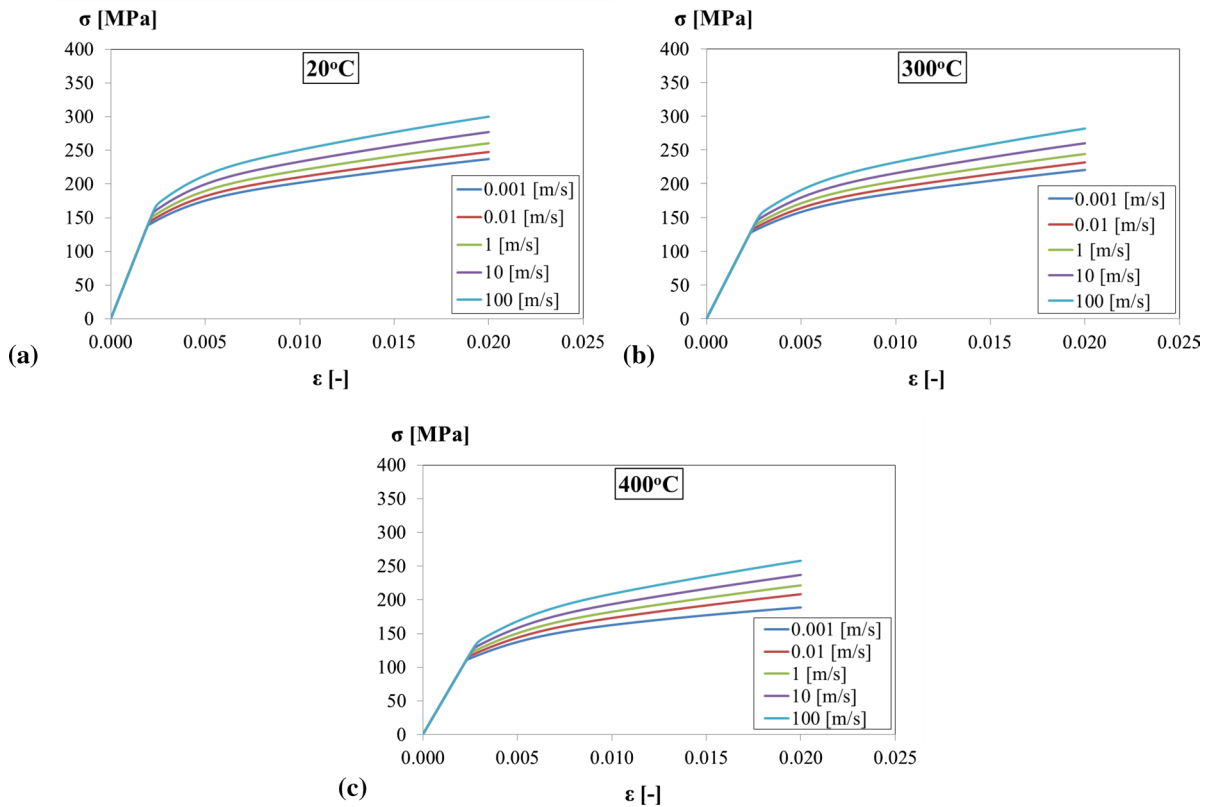
Fig. 6 The stress–strain curves for strain rates in a range of 0.001–10 s^{-1} for temperatures; 20 °C (**a**), 300 °C (**b**) and 400 °C (**c**)
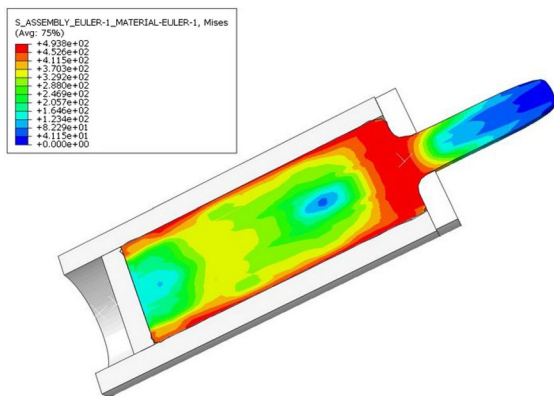

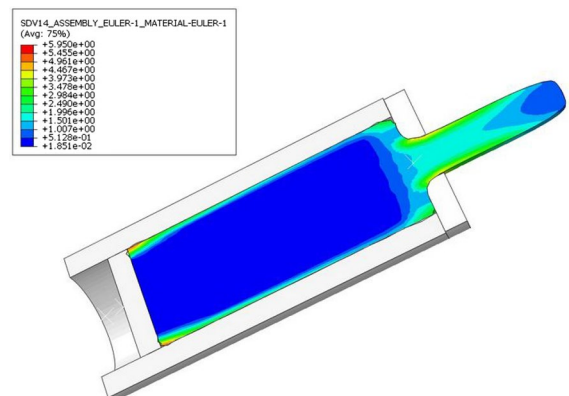**Fig. 7** The von-Mises stress [MPa] distribution in the extruded material

Fig. 8 The equivalent plastic strain [-] distribution in the extruded material

6 Summary and conclusions

The three-dimensional thermo-mechanical coupled Eulerian–Lagrangian analysis was used in order to simulate the KOBO extrusion process of the AMG-6 alloy. The elastic-viscoplastic unified Bodner–Partom model including the large displacements was applied here. The model parameters

Fig. 9 The comparison of plastic zones in a numerical simulation (**a**) and its experimental verification (**b** [102], **c**)
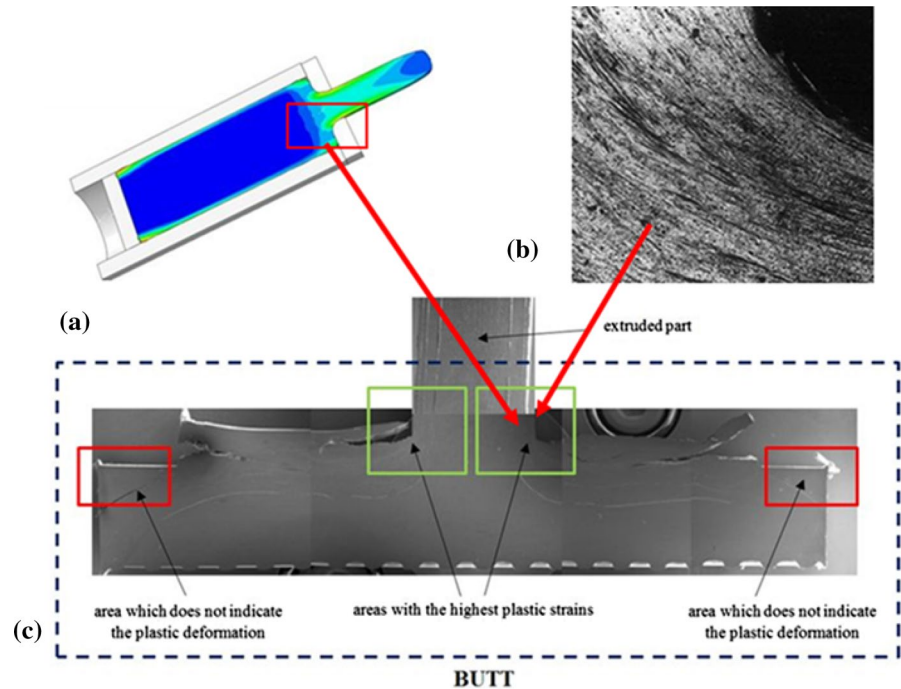
were selected on the basis of the literature review. In numerical calculations, the extruded material was modelled using the Eulerian mesh and the tools (die, recipient and punch) were defined as rigid bodies using the Lagrangian mesh. The explicit integration of constitutive equations was used here.

For the Bodner–Partom material model the user procedure was written and later on it was linked to the commercial FEM software. The correctness of the user subroutine was checked on several elastic–plastic benchmark tests.

Different shapes of Eulerian domains and variously tuned meshes were tested. The cylindrical Eulerian space with the mesh thickening to the core was chosen as one which provides the best results. On the basis of results obtained, the following conclusions can be drawn.

(1) The CEL method enables to model the KOBO extrusion process and obtain reliable results. Contrary to the Lagrangian approach, remeshing is not necessary.

(2) The proper modelling of the KOBO extrusion applying the user procedure extends the knowledge about strain hardening and temperature sof-

tening in extruded material, and enables to set-up experimental conditions of the process.

(3) The coupled thermomechanical problem requires definition of the material data for the whole range of temperatures which occur in the process.

(4) The knowledge concerning the material characteristic, including the material hardening can optimize the process and select the proper die frequency and amplitude in order to avoid technical problems associated with the material extrusion and the die damage.

Declarations

References

1. Ryzińska G, Skrzat A (2015) Modeling of 1100 aluminum extrusion process at high strain-rates. Sci Bull, Series C, Fascicle: Mech Tribol Mach Manuf Technol 29:70–75

2. Forni D, Mazzucato F, Valente A, Cadoni E (2021) High strain-rate behavior of as-cast and as-build Inconel 718 alloys at elevated temperatures. Mech Mater. https://doi.org/10.1016/j.mechmat.2021.103859

3. Field JE, Walley SM, Proud WG, Goldrein HT, Siviour CR (2004) Review of experimental techniques for high rate deformation and shock studies. Int J Impact Eng 30(7):725–775. https://doi.org/10.1016/j.ijimpeng.2004.03.005

4. Zhang H, Dong X, Du D, Wang Q (2013) A unified physically based crystal plasticity model for FCC metals over a wide range of temperatures and strain rates. Mater Sci Eng 564:431–441. https://doi.org/10.1016/j.msea.2012.12.001

5. Bodner SR (2002) Unified plasticity for engineering applications. Springer, New York

6. Bodner SR (2005) Plasticity over a wide range of strain rates and temperatures. Arch Mech 57:73–80

7. Estrin Y, Mecking H (1986) An extension of the Bodner–Partom model of plastic deformation. Int J Plast 2(1):73–85. https://doi.org/10.1016/0749-6419(86)90017-3

8. Luque J, Campoamor-Stursberg R (2009) Geometrical foundations of plasticity yield criteria. A unified theory. Materials Science. arXiv:0912.0426v1

9. Estrin Y, Molinari A, Mercier S (1997) The role of rate effects and of thermomechanical coupling in shear localization. J Eng Mater Technol 119(4):322–331. https://doi.org/10.1115/1.2812265

10. Zerilli FJ, Armstrong RW (1987) Dislocation-mechanics-based constitutive relations for material dynamic calculations. J Appl Phys. https://doi.org/10.1063/1.338024

11. Gupta AK, Krishnamurthy HN, Puranik P, Singh SK, Balu A (2014) An exponential strain dependent Rusinek-Klepaczko model for flow stress prediction in austenitic stainless steel 304 at elevated temperatures. J Mater Res Technol 3(4):370–377. https://doi.org/10.1016/j.jmrt.2014.08.001

12. Rusinek A, Zaera R, Klepaczko JR (2007) Constitutive relations in 3-D for a wide range of strain rates and temperatures–application to mild steels. Int J Solids Struct 44(17):5611–5634. https://doi.org/10.1016/j.ijsolstr.2007.01.015

13. Simon P, Demarty Y, Rusinek A, Voyiadjis GZ (2018) Material behavior description for a large range of strain rates from low to high temperatures: application to high strength steel. Metals. https://doi.org/10.3390/met8100795

14. Nemat-Nasser S, Okinaka T, Ni L (1998) A physically-based constitutive model for bcc crystals with application to polycrystalline tantalum. J Mech Phys Solids 46(6):1009–1038. https://doi.org/10.1016/S0022-5096(97)00064-1

15. Follansbee PS, Kocks UF (1998) A constitutive description of the deformation of copper based on the use of the mechanical threshold stress as an internal state variable. Acta Metall 36(1):81–93. https://doi.org/10.1016/0001-6160(88)90030-2

16. Follansbee PS, Gray TG (1989) An analysis of the low temperature, low and high strain-rate deformation of Ti−6Al−4V. Metall Trans A 20:863–874. https://doi.org/10.1007/BF02651653

17. Molinari A, Ravichandran G (2005) Constitutive modeling of high-strain-rate deformation in metals based on the evolution of an effective microstructural length. Mech Mater 37(7):737–752. https://doi.org/10.1016/j.mechmat.2004.07.005

18. Burley M, Campbell JE, Clyne TW (2018) Johnson-Cook parameter evaluation from ballistic impact data via iterative FEM modelling. Int J Impact Eng 112:180–192. https://doi.org/10.1016/j.ijimpeng.2017.10.012

19. Murugesan M, Jung DW (2019) Johnson Cook material and failure model parameters estimation of AISI-1045 medium carbon steel for metal forming applications. Materials. https://doi.org/10.3390/ma12040609

20. Devotta AM, Sivaprasad PV, Beno T, Eynian M, Hjertig K, Magnevall M, Lundblad M (2019) A modified Johnson-Cook model for ferritic-pearlitic steel in dynamic strain aging regime. Metals. https://doi.org/10.3390/met9050528

21. Miller A (1976) An inelastic constitutive model for monotonic, cyclic, and creep deformation: Part I. Equations development and analytical procedures. J. Engng. Mater. Technol. 98(2):97–105. https://doi.org/10.1115/1.3443367

22. Bodner S, Partom Y (1975) Constitutive equations for elastic-viscoplastic strain-hardening materials. J Appl Mech 42:385–389. https://doi.org/10.1115/1.3423586

23. Delobelle P (1988) Sur les lois de comportement viscoplastique à variables internes. Rev Phys Appl 23:1–61. https://doi.org/10.1051/rphysap:019880023010100

24. Kocks UF (1976) Laws for work-hardening and low-temperature creep. J Engng Mater Technol 98(1):76–85. https://doi.org/10.1115/1.3443340

25. Krempl E, McMahon JJ, Yao D (1986) Viscoplasticity based on overstress with a differential growth law for the equilibrium stress. Mech. Mater. 5(1):35–48. https://doi.org/10.1016/0167-6636(86)90014-1

26. Chaboche JL (1989) Constitutive equations for cyclic plasticity and cyclic viscoplasticity. Int J Plast 5(3):247–302. https://doi.org/10.1016/0749-6419(89)90015-6

27. Ahmed R, Barrett PR, Hassan T (2016) Unified viscoplasticity modeling for isothermal low-cycle fatigue and fatigue-creep stress–strain responses of Haynes 230. Int

J Plast 88–89:131–145. https://doi.org/10.1016/j.ijsolstr.2016.03.012

28. Perzyna P (1964) On the constitutive equations for work-hardening and rate sensitive plastic materials. Bull Acad Polon Sci Série Sci Technol. 12(4):199–206

29. Kłosowski P, Mleczek A (2014) Parameters' identification of perzyna and chaboche viscoplastic models for aluminum alloy at temperature of 120°C. Eng Trans 62(3):291–305

30. Lazari M, Sanavia L, di Prisco C, Pisano F (2019) Predictive potential of Perzyna viscoplastic modelling for granular geomaterials. Int J Numer Anal Methods Geomech 43(2):544–567. https://doi.org/10.1002/nag.2876

31. Chaboche JL (2008) A review of some plasticity and viscoplasticity constitutive theories. Int J Plast 24(10):1642–1693. https://doi.org/10.1016/j.ijplas.2008.03.009

32. Arnold S, Saleeb A (1994) On the thermodynamic framework of generalized coupled thermoelastic–viscoplastic-damage modeling. Int J Plast 10(3):263–278. https://doi.org/10.1016/0749-6419(94)90003-5

33. Saleeb A, Arnold S, Castelli M, Wilt T, Graf W (2001) A general hereditary multimechanism-based deformation model with application to the viscoelastoplastic response of titanium alloys. Int J Plast 17(10):1305–1350. https://doi.org/10.1016/S0749-6419(00)00086-3

34. Abed FH (2005) Physically based multiscale-viscoplastic model for metals and Physically based multiscale-viscoplastic model for metals and steel alloys: theory and computation steel alloys: theory and computation. Luisiana State University, Lafayette

35. Hartmann G (1990) Comparison of the uniaxial behavior of the inelastic constitutive models of Miller and Walker by numerical experiments. Int J Plast 6(2):189–206. https://doi.org/10.1016/0749-6419(90)90021-6

36. Delobelle P, Robinet P, Bocher L (1995) Experimental study and phenomenological modelization of ratcheting under uniaxial and biaxial loading on an austenitic stainless steel. Int J Plast 11(4):295–330. https://doi.org/10.1016/S0749-6419(95)00001-1

37. Heeres OM, Suiker ASJ, de Borst R (2002) A comparison between the Perzyna viscoplastic model and the consistency viscoplastic model. Eur J Mech A Solids 21(1):1–12. https://doi.org/10.1016/S0997-7538(01)01188-3

38. Chen W, Wang F, Kitamura T, Feng M (2017) A modified unified viscoplasticity model considering time-dependent kinematic hardening for stress relaxation with effect of loading history. Int J Mech Sci 133:883–892. https://doi.org/10.1016/j.ijmecsci.2017.09.048

39. Klosowski P, Zerdzicki K, Woznica K (2017) Identification of Bodner–Partom model parameters for technical fabrics. Comput Struct 187:114–121. https://doi.org/10.1016/j.compstruc.2017.03.022

40. Sagradow I, Schob D, Roszak R, Maasch P, Sparr H, Ziegenhorn M (2020) Experimental investigation and numerical modelling of 3D printed polyamide 12 with viscoplasticity and a crack model at different strain rates. Mater Today Commun. https://doi.org/10.1016/j.mtcomm.2020.101542

41. Andersson H (2003) An implicit integration of the Bodner–Partom constitutive equations. Comput Struct 81:1405–1414. https://doi.org/10.1016/S0045-7949(03)00019-1

42. Ryzińska G, Skrzat A (2015) Designing an impact energy-absorbing device: numerical simulations. RUTMech 87(4):349–357. https://doi.org/10.7862/rm.2015.34

43. Huang S, Khan AS (1992) Modeling the mechanical behaviour of 1100-0 aluminum at different strain rates by the Bodner–Partom model. Int J Plast 8(5):501–517. https://doi.org/10.1016/0749-6419(92)90028-B

44. Chan KS (1988) The constitutive representation of high-temperature creep damage. Int J Plast 4(4):355–370. https://doi.org/10.1016/0749-6419(88)90024-1

45. Avila AF, Krishina TK (1999) Non-linear analysis of laminated metal matrix composites by an integrated micro/macro-mechanical model. J Braz Soc Mech Sci. https://doi.org/10.1590/S0100-73861999000400006

46. Zairi F, Nait-Abdelaziz M, Woźnica K, Gloaguen JM (2005) Constitutive equations for the viscoplastic-damage behaviour of a rubber-modified polymer. Eur J Mech A/Solids 24:169–182. https://doi.org/10.1016/j.euromechsol.2004.11.003

47. Molinari A, Mercier S, Jacques N (2014) Dynamic failure of ductile materials. Procedia IUTAM 10:201–220. https://doi.org/10.1016/j.piutam.2014.01.019

48. Ambroziak A (2005) Numerical modelling of elasto-viscoplastic Bodner–Partom constitutive equations. Task Quart 9(4):461–473

49. Pyrz M, Zairi F (2007) Identification of viscoplastic parameters of phenomenological constitutive equations for polymers by deterministic and evolutionary approach. Model Simul Mater Sci Eng 15(2):85–103

50. Sands M, Chandler HW, Guz IA, Zhuk YA (2010) Extending the Bodner–Partom model to simulate the response of materials with extreme kinematic hardening. Arch Appl Mech. https://doi.org/10.1007/s00419-009-0307-0

51. Rubin MB, Bodner SR (2002) A three-dimensional nonlinear model for dissipative response of soft tissues. Int J Solids Struct 39(19):5081–5090

52. Kłosowski P, Zagubień A, Woznica K (2004) Investigation on rheological properties of technical fabric "Panama." Arch Appl Mech 73:661–681. https://doi.org/10.1007/s00419-004-0321-1

53. Kłosowski P, Zerdzicki K, Woznica K (2019) Influence of artificial thermal ageing on polyester-reinforced and polyvinyl chloride coated AF9032 technical fabric. Text Res J 89(21–22):4632–4646. https://doi.org/10.1177/0040517519839934

54. Viswanath A, Dieringa H, Ajith Kumar KK, Pillai UTS, Pai BC (2015) Investigation on mechanical properties and creep behavior of stir cast AZ91-SiC$_p$ composites. J Magnes Alloy 3(1):16–22. https://doi.org/10.1016/j.jma.2015.01.001

55. Cui-Hong Z, Xue-peng C, Sheng-jie J, Xin-xin X, Tong-chao Z, Yao F (2019) Viscoelastoplastic compaction properties of cement-emulsified asphalt mixture based on Bodner–Partom model. China J Highw Transp 32(7):41–48

56. Liu M, Huang X, Wu Y, Chen C, Huang F (2019) Numerical simulations of the damage evolution for plastic-bonded explosives subjected to complex stress states. Mech Mater. https://doi.org/10.1016/j.mechmat.2019.103179

57. Ambroziak A, Kłosowski P (2007) Determining the viscoplastic parameters of rubber-toughened plastics. Task Quart 12(1):35–43

58. Bocko J, Nohajová V, Šarloši J (2015) Simulation of material behaviour by Bodner–Partom model. Am J Mech Eng 3(6):181–185. https://doi.org/10.12691/ajme-3-6-5

59. Skrzat A (2011) Fuzzy logic application to strain-stress analysis in selected elastic-plastic material models. Arch Metall Mater 56(2):559–568. https://doi.org/10.1016/S0749-6419(95)00016-X

60. Cecot W (2006) Adaptive analysis of inelastic problems with Bodner–Partom constitutive model. Comput Assist Methods Eng Sci 13(4):513–521

61. Bartczak L (2012) Mathematical analysis of a thermo-visco-plastic model with Bodner–Partom constitutive equations. J Math Anal Appl 385(2):961–974. https://doi.org/10.1016/j.jmaa.2011.07.023

62. Dombrovsky A (1992) Incremental constitutive equations for miller and Bodner–Partom viscoplastic models. Comput Struct 44(5):1065–1072. https://doi.org/10.1016/0045-7949(92)90329-X

63. Senchenkov IK, Tabieva GA (1996) Determination of the parameters of the Bodner–Partom model for thermoviscoplastic deformation of materials. Int Appl Mech 32:132–139. https://doi.org/10.1007/BF02086653

64. Bonora N, Testa G, Ruggiero A, Iannitti G, Mortazavi N, Hörnqvist M (2015) Numerical simulation of dynamic tensile extrusion test of OFHC copper. J Dyn Behav Matter 1:136–152. https://doi.org/10.1007/s40870-015-0013-7

65. Bochniak W, Korbel A, Ostachowski P, Ziółkiewicz S, Borowski J (2013) Wyciskanie metali i stopów metodą KOBO. Obrób Plast Met 24(2):83–97

66. Pawłowska B, Śliwa RE, Zwolak M (2019) Possibilities to obtain products from 2024 and 7075 chips in the process of consolidation by KOBO extrusion. Arch Metall Mater 64(4):1213–1221. https://doi.org/10.24425/amm.2019.130083

67. Zwolak M, Śliwa RE (2017) Fizyczne modelowanie plastycznego płynięcia w procesie wyciskania metodą KOBO z użyciem matryc o różnej geometrii. Obrób Plast Met 28(4):317–330

68. Dutkiewicz J, Kalita D, Maziarz W, Tański T, Borek W, Ostachowski P, Faryna M (2020) Effect of KOBO extrusion and following cyclic forging on grain refinement of Mg–9Li–2Al–0.5Sc alloy. Met Mater Int 26:1004–1014. https://doi.org/10.1007/s12540-019-00350-y

69. Korbel A, Pieła K, Ostachowski P, Łagoda M, Błaż L, Bochniak W, Pawlyta M (2018) Structural phenomena induced in the course of and post low-temperature KOBO extrusion of AA6013 aluminum alloy. Mater Sci Eng 710:349–358. https://doi.org/10.1016/j.msea.2017.10.095

70. Pieła K, Błaż L, Jaskowski M (2013) Effects of extrusion parameters by KoBo method on the mechanical

properties and microstructure of aluminum. Arch Metall Mater 58(3):683–689. https://doi.org/10.2478/amm-2013-0055

71. Balawender T, Zwolak M, Bąk Ł (2020) Experimental analysis of mechanical characteristics of KOBO extrusion method. Arch Metall Mater 65(2):615–619. https://doi.org/10.24425/amm.2020.132800

72. Hyvärinen M, Jabeen R, Käarki T (2020) The modelling of extrusion processes for polymers—a review. Polymers. https://doi.org/10.3390/polym12061306

73. Ryzińska G, Gieleta R (2016) Experimental and numerical modeling of the extrusion process in 1050A aluminum alloy for design of impact energy-absorbing devices. Strength Mater 48:551–560. https://doi.org/10.1007/s11223-016-9797-5

74. Boparai KS, Singh R, Singh H (2016) Modeling and optimization of extrusion process parameters for the development of Nylon6–Al–Al$_2$O$_3$ alternative FDM filament. Prog Addit Manuf 1:115–128. https://doi.org/10.1007/s40964-016-0011-x

75. Ryzińska G, Skrzat A, Śliwa RE (2015) Coupled Eulerian-Lagrangian approach in simulation of extrusion process. Metal Forming 26(1):73–92

76. Kowalczyk-Gajewska K, Stupkiewicz S (2013) Modelling of texture evolution in KOBO extrusion process. Arch Metall Mater 58(1):113–118. https://doi.org/10.2478/v10172-012-0160-y

77. Gusak A, Danielewski M, Korbel A, Bochniak M, Storozhuk N (2014) Elementary model of severe plastic deformation by KoBo process. J Appl Phys. https://doi.org/10.1063/1.4861870

78. Wójcik M, Skrzat A (2021) The coupled Eulerian-Lagrangian analysis of the KOBO extrusion process. ASTRJ 15(1):197–208. https://doi.org/10.12913/22998624/131663

79. Ahmed R, Barrett PR, Hassan T (2016) Unified viscoplasticity modeling for isothermal low-cycle fatigue and fatigue-creep stress–strain responses of Haynes 230. Int J Solid Struct 88–89:131–145. https://doi.org/10.1016/j.ijsolstr.2016.03.012

80. Zaera R, Fernández-Sáez J (2006) An implicit consistent algorithm for the integration of thermoviscoplastic constitutive equations in adiabatic conditions and finite deformations. Int J Solid Struct 43(6):1594–1612. https://doi.org/10.1016/j.ijsolstr.2005.03.070

81. ALE adaptive meshing and remapping in Abaqus/Explicit. https://abaqus-docs.mit.edu/2017/English/SIMACAEANLRefMap/simaanl-c-aleremesh.htm. Accessed 20 December 2021

82. Kolkailah FA, McPhate AJ (1990) Bodner–Partom constitutive model and nonlinear finite element analysis. J Eng Mater Technol 112(3):287–291. https://doi.org/10.1115/1.2903325

83. Kłosowski P, Woźnica K (1999) Problems of identification of material parameters for different types of viscoplastic constitutive equations. Engng Trans 47(2):135–144

84. Cocchetti G, Pagani M, Perego U (2013) Selective mass scaling and critical time-step estimate for explicit dynamics analyses with solid-shell elements. Comput

Struct 127:39–52. https://doi.org/10.1016/j.compstruc.2012.10.021

85. Okereke M, Keates S (2018) Finite element applications. A practical guide to the FEM process. Springer, Cham

86. Perez N (2017) Theory of elasticity. Springer, Cham

87. Pila AW (2020) Introduction to lagrangian dynamics. Springer, Cham

88. Wang T, Zhou H, Zhang X, Ran T (2018) Stability of an explicit time-integration algorithm for hybrid tests, considering stiffness hardening behavior. Earthq Eng Eng Vib 17:595–606. https://doi.org/10.1007/s11803-018-0465-6

89. Ducobu F, Rivière-Lorphèvre E, Filippi E (2016) Application of the Coupled Eulerian-Lagrangian (CEL) method to the modeling of orthogonal cutting. Eur J Mech A Solids 59:58–66. https://doi.org/10.1016/j.euromechsol.2016.03.008

90. Ducobu F, Arrazola P-J, Rivière-Lorphèvre E, Ortiz de Zarate G, Madariaga A, Filippi E (2018) The CEL method as an alternative to the current modelling approaches for Ti6Al4V orthogonal cutting simulation. Procedia CIRP 58:245–250. https://doi.org/10.1016/j.procir.2017.03.188

91. Salloomi KN, Al-Sumaidae S (2021) Coupled Eulerian-Lagrangian prediction of thermal and residual stress environments in dissimilar friction stir welding of aluminum alloys. J Adv Join Process. https://doi.org/10.1016/j.jajp.2021.100052

92. Chauhan P, Jain R, Pal SK, Singh SB (2018) Modeling of defects in friction stir welding using coupled Eulerian and Lagrangian method. J Manuf Process 34A:158–166. https://doi.org/10.1016/j.jmapro.2018.05.022

93. Ko J, Jeong S, Kim J (2017) Application of a coupled Eulerian-Lagrangian technique on constructability problems of site on very soft soil. Appl Sci. https://doi.org/10.3390/app7101080

94. Qiu G, Henke S, Grabe J (2009) Applications of Coupled Eulerian-LagrangianMethod to Geotechnical Problems with Large Deformations. https://www.semanticscholar.org/paper/Applications-of-Coupled-Eulerian-Lagrangian-Method-Qiu-Henke/314d8d71f6641c8d57d98ebc27a802380db44bb6. Accessed 20 December 2021

95. Benson DJ, Okazawa S (2004) Contact in a multi-material Eulerian finite element formulation. Comput Methods Appl Mech Eng 193:4277–4298. https://doi.org/10.1016/j.cma.2003.12.061

96. Gao Y, Ko JH, Lee HP (2018) 3D coupled Eulerian-Lagrangian finite element analysis of end milling. Int J Adv Manuf Technol 98:849–857. https://doi.org/10.1007/s00170-018-2284-3

97. Behrens B-A, Chugreev A, Bohne F, Lorenz R (2019) Approach for modelling the Taylor-Quinney coefficient of high strength steels. Procedia Manuf 29:464–471. https://doi.org/10.1016/j.promfg.2019.02.163

98. Cocchetti G, Pagani M, Perego U (2015) Selective mass scaling for distorted solid-shell elements in explicit dynamics: optimal scaling factor and stable time step estimate. Int J Numer Meth Engng 101(9):700–731. https://doi.org/10.1002/nme.4829

99. Methods of speeding up the analysis. https://abaqus-docs.mit.edu/2017/English/SIMACAEGSARefMap/simagsa-c-qsimetspeedanal.htm. Accessed 20 December 2021

100. Benson DJ (1995) A multi-material Eulerian formulation for the efficient solution of impact and penetration problems. Comput Mech 15:558–571. https://doi.org/10.1007/BF00350268

101. Selecting an amplitude type to define. http://dsk-016-1.fsid.cvut.cz:2080/v6.12/books/usi/default.htm?startat=pt06ch57s03.html. Accessed 20 December 2021

102. Korbel A, Pospiech J, Bochniak W, Tarasek A, Ostachowski P, Bonarski J (2011) New structural and mechanical features of hexagonal materials after room temperature extrusion using KoBo method. Int J Mat Res (formerly Z Metallkd) 102:464–473. https://doi.org/10.3139/146.110490

103. Feigenbaum HP, Dugdale J, Dafalias YF, Kourousis KI, Plesek J (2012) Multiaxial ratcheting with advanced kinematic and directional distortional hardening rules. Int J Soli Struct 49(22):3063–3076. https://doi.org/10.1016/j.ijsolstr.2012.06.006

104. Wójcik M, Skrzat A (2021) Identification of Chaboche-Lemaitre combined isotropic-kinematic hardening model parameters assisted by the fuzzy logic analysis. Acta Mech 232(2):685–708. https://doi.org/10.1007/s00707-020-02851-z

105. Skrzat A, Wójcik M (2020) An identification of the material hardening parameters for cyclic loading—experimental and numerical studies. Arch Metall Mater 65(2):779–786. https://doi.org/10.24425/amm.2020.132820